


Mid-Holocene rainfall seasonality and ENSO dynamics over the south-western Pacific

Cinthy Nava-Fernandez¹  | Tobias Braun² | Chelsea L. Pederson¹ | Bethany Fox³ | Adam Hartland⁴ | Ola Kwiecien⁵ | Sebastian N. Höpker⁴ | Stefano Bernasconi⁶ | Madalina Jaggi⁶ | John Hellstrom⁷ | Fernando Gázquez^{8,9} | Amanda French⁴ | Norbert Marwan² | Adrian Immenhauser^{1,10} | Sebastian F. M. Breitenbach⁵

¹Sediment- and Isotope Geology, Institute for Geology, Mineralogy and Geophysics, Ruhr-Universität Bochum, Bochum, Germany

²Potsdam Institute for Climate Impact Research (PIK), Member of the Leibniz Association, Potsdam, Germany

³Department of Biological and Geographical Sciences, School of Applied Sciences, University of Huddersfield, Huddersfield, UK

⁴Environmental Research Institute, School of Science, Faculty of Science and Engineering, University of Waikato, Hamilton, Waikato, New Zealand

⁵Department of Geography and Environmental Sciences, Northumbria University, Newcastle upon Tyne, UK

⁶Department of Earth Sciences, ETH Zurich, Zurich, Switzerland

⁷School of Earth Sciences, The University of Melbourne, Melbourne, Victoria, Australia

⁸Department of Biology and Geology, Universidad de Almería, Almería, Spain

⁹Andalusian Centre for the Monitoring and Assessment of Global Change (CAESCG), University of Almería, Almería, Spain

¹⁰Fraunhofer Research Institution for Energy Infrastructures and Geothermal Systems IEG, Bochum, Germany

Correspondence

Cinthy Nava-Fernandez, Sediment- and Isotope Geology, Institute for Geology, Mineralogy and Geophysics, Ruhr-Universität Bochum, Universitätsstr. 150, Bochum 44801, Germany.
Email: cinthy.navafernandez@gmail.com

Funding information

Junta de Andalucía-FEDER 2022–2026, Grant/Award Number: RYC-PPI2021-01; Ramón y Cajal fellowship, Grant/Award Number: RYC2020-029811-I PPIT-UAL; Rutherford Discovery Fellowship programme, Grant/Award Number: RDF-UOW1601; German Academic Exchange Service (DAAD); Te Apārangi Royal Society of New Zealand, Grant/Award Number: RIS-UOW1501; European Union's Horizon 2020 Research and Innovation programme through a Marie Skłodowska-Curie grant, Grant/Award Number: 691037

Abstract

El Niño–Southern Oscillation dynamics affect global weather patterns, with regionally diverse hydrological responses posing critical societal challenges. The lack of seasonally resolved hydrological proxy reconstructions beyond the observational era limits our understanding of boundary conditions that drive and/or adjust El Niño–Southern Oscillation variability. Detailed reconstructions of past El Niño–Southern Oscillation dynamics can help modelling efforts, highlight impacts on disparate ecosystems and link to extreme events that affect populations from the tropics to high latitudes. Here, mid-Holocene El Niño–Southern Oscillation and hydrological changes are reconstructed in the south-west Pacific using a stalagmite from Niue Island, which represents the period 6.4–5.4 ka BP. Stable oxygen and carbon isotope ratios, trace elements and greyscale data from a U/Th-dated and layer counted stalagmite profile are combined to infer changes in local hydrology at sub-annual to multi-decadal timescales. Principal component analysis reveals seasonal-scale hydrological changes expressed as variations in stalagmite growth patterns and geochemical characteristics. Higher levels of host rock-derived elements (Sr/Ca and U/Ca) and higher $\delta^{18}\text{O}$ and $\delta^{13}\text{C}$ values are observed in dark, dense calcite laminae deposited during the dry season, whereas

This is an open access article under the terms of the [Creative Commons Attribution](https://creativecommons.org/licenses/by/4.0/) License, which permits use, distribution and reproduction in any medium, provided the original work is properly cited.

© 2024 The Authors. *The Depositional Record* published by John Wiley & Sons Ltd on behalf of International Association of Sedimentologists.

during the wet season, higher concentrations of soil-derived elements (Zn/Ca and Mn/Ca) and lower $\delta^{18}\text{O}$ and $\delta^{13}\text{C}$ values are recorded in pale, porous calcite laminae. The multi-proxy record from Niue shows seasonal cycles associated with hydrological changes controlled by the positioning and strength of the South Pacific Convergence Zone. Wavelet analysis of the greyscale record reveals that El Niño–Southern Oscillation was continuously active during the mid-Holocene, with two weaker intervals at 6–5.9 and 5.6–5.5 ka BP. El Niño–Southern Oscillation especially affects dry season rainfall dynamics, with increased cyclone activity that reduces hydrological seasonality during El Niño years.

KEYWORDS

ENSO, mid-Holocene, multi-proxy reconstruction, Niue Island, speleothems

1 | INTRODUCTION

Tropical Pacific dynamics play a key role in the global climate. The South Pacific Convergence Zone (SPCZ) is the dominant climate feature that channels convective rainfall in the South Pacific at seasonal scale (Brown et al., 2020). At interannual scales (2–8 years), climate variability is controlled by the coupled ocean–atmosphere phenomenon El Niño–Southern Oscillation (ENSO) (Folland et al., 2002; Timmermann et al., 2018). These climate features modulate rainfall amount as well as the frequency and intensity of extreme weather events (e.g. tropical cyclones and droughts). Thus, the SPCZ and ENSO greatly impact the ecosystems and lives of the Pacific islanders and the east and west coasts of the Pacific basin (CSIRO & Australian Bureau of Meteorology, 2011). A range of projections from climate models have forecast increased vulnerability of the tropical Pacific islands to the impacts of anthropogenically driven warming (CSIRO & Australian Bureau of Meteorology, 2011). The need to generate accurately dated, high-resolution long-term records, from underrepresented regions is unquestionable. Specifically, new ENSO past variability records are critical for evaluating the robustness of climate models and forecasts of regional and global climate change (Cane, 2005; Capotondi et al., 2015; Emile-Geay et al., 2016).

Detailed knowledge of long-term ENSO variability is fundamental to interpreting the observed dynamics, and to be able to separate natural variability from external forcings, including those induced by human activities. Climate archives such as fossil corals show evidence that ENSO activity has been present since the Pliocene (Watanabe et al., 2011) and through the Quaternary (Tudhope et al., 2001; Cobb et al., 2013). The study of ENSO variability is particularly relevant during the Holocene because this period is when human activity became a significant forcing mechanism at global scale. Here the focus is on the

mid-Holocene hydrological conditions, a period for which no continuous high-resolution ENSO records are available from the South Pacific.

Diverse studies have reconstructed ENSO dynamics during the Holocene using climate archives such as marine sediments (Koutavas et al., 2006), corals (Tudhope et al., 2001; Cobb et al., 2013), clastic lake sediments (Moy et al., 2002; Conroy et al., 2008) and speleothems (Chen et al., 2016). The resolution of these records ranges from multi-decadal to monthly, but they often represent discrete, shorter time intervals rather than continuous intervals. Several studies from the Pacific suggested that ENSO variability was reduced in terms of intensity and frequency during the mid-Holocene. These include records from the eastern Pacific, such as lake sediments from Ecuador and the Galapagos (Rodbell et al., 1999; Conroy et al., 2008), foraminifera (Koutavas & Joanides, 2012) and western Pacific records, for example pollen from Australasia (Shulmeister & Lees, 1995) and corals from Papua New Guinea (Tudhope et al., 2001). According to a numerical model (Clement et al., 2000), this reduction in ENSO strength during the mid-Holocene was a response to orbitally driven seasonality changes. However, other authors whose records indicated reduced mid-Holocene ENSO variance suggested that the driver was a change in the equatorial Pacific mean state (Cobb et al., 2013; Chen et al., 2016; White et al., 2018).

Speleothems (secondary cave carbonates) offer a wide range of environmentally sensitive proxies and accurate age control. Their near-ubiquitous distribution (Fairchild & Baker, 2012) and potential temporal resolution ranging from intra-seasonal (Ridley et al., 2015; Braun et al., 2023) to orbital (Cheng et al., 2016) make speleothems attractive palaeoenvironmental archives. Speleothem-derived stable oxygen isotope ratios ($\delta^{18}\text{O}$) can provide information about regional moisture history (e.g. rainfall amount and water vapour source) (Lachniet, 2009; Breitenbach

et al., 2010), whereas stable carbon isotope ratios ($\delta^{13}\text{C}$) can reflect the interaction of soil CO_2 and variations in local infiltration processes inherent to the karst system (Genty et al., 2003; Fohlmeister et al., 2020). The interpretation of the $\delta^{13}\text{C}$ signal can be further informed by trace element ratios (e.g. Mg/Ca, Sr/Ca; Magiera et al., 2019; Fohlmeister et al., 2020). Processes such as prior carbonate precipitation (PCP) control trace element ratios in the stalagmite. It occurs when the Ca-saturated solution degasses CO_2 by encountering air-filled voids along its flow path through the epikarst and at the cave ceiling, which leads to carbonate precipitation, enrichment of elements with distribution coefficients <1 in dripwater and (carbon and oxygen) isotope fractionation (Fairchild et al., 2000). Less frequently used environmental proxies include variations in physical features such as speleothem density, fabrics, colour and lamina thickness, which are a function of hydrology, karst conditions, drip rate and dripwater chemistry (Kendall & Broughton, 1978; Frisia et al., 2000; Walczak et al., 2015). These processes are reflected in speleothem growth rate and seasonal depositional changes (dry/wet) and can be observed by using high-resolution imaging (Faraji et al., 2021). Accounting for these features can improve the interpretation of geochemical data.

Presented here is a seasonally resolved mid-Holocene (6.4–5.4 ka BP) stalagmite record from Niue Island in the south-western Pacific. This multi-proxy approach

combines $\delta^{18}\text{O}$ and $\delta^{13}\text{C}$ values, trace element concentrations and physical properties. The research objectives include (a) characterisation of the nature of the observed speleothem laminae; (b) identification of the environmental controls on the physical and geochemical proxies; (c) establishing a chronology for the proxy records; and (d) extraction of the fundamental periodicities from the observed proxy variability. Principal component analysis (PCA) was used to identify clusters/groups of strongly co-varying proxies and infer incorporation mechanisms from these results. Wavelet analysis was performed to decompose the proxy time series into the time and frequency domains to extract the fundamental periods in the record.

2 | GEOGRAPHIC SETTING AND CLIMATE

Niue Island is a carbonate edifice located in the south-western tropical Pacific (S 19°03', W 169°55') (Figure 1). The carbonate build-up that forms Niue Island consists of partially dolomitised, shallow water reefal limestone that reaches a stratigraphic thickness of *ca* 400 m and rests on a volcanic, early middle Miocene basement. The uppermost platform consists of up to 20 m thick aragonite and calcite deposits (Aharon et al., 2006). The island reaches a maximum altitude of *ca* 60 m a.s.l. and hosts numerous caves, particularly in the Mutulau reefal limestone and coastal

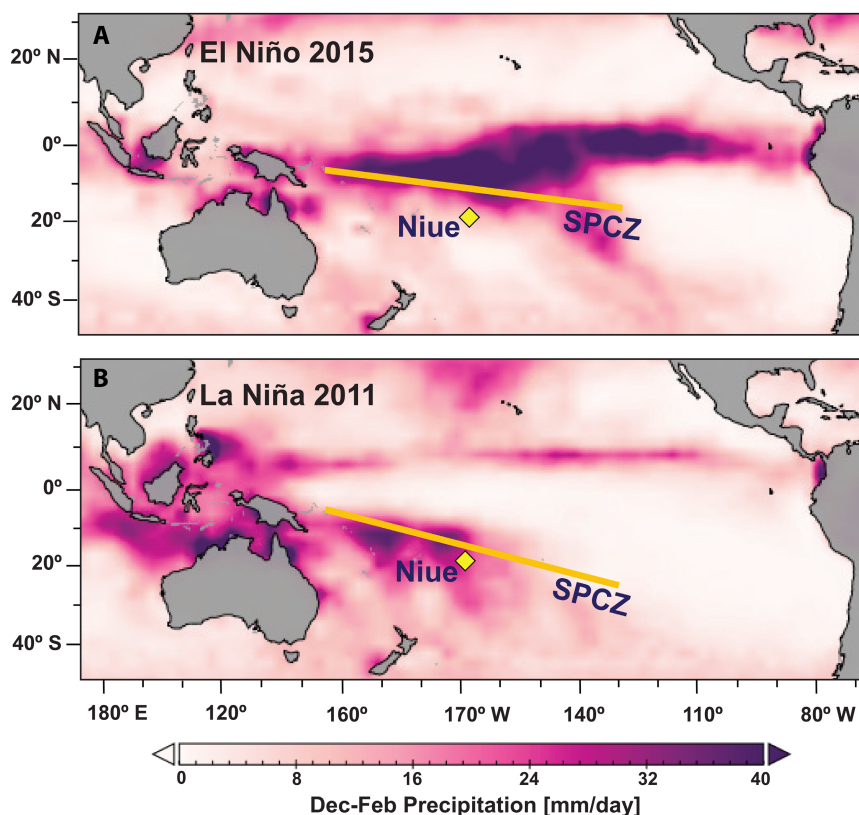


FIGURE 1 Austral summer (December–February) daily precipitation across the Pacific. The yellow lines highlight the position of the South Pacific Convergence Zone (SPCZ) during two strong ENSO events: (A) El Niño 1998; and (B) La Niña 2011. The yellow diamond indicates the location of Niue Island. NOAA Climate Data Record (CDR) of GPCP Satellite-Gauge Combined Precipitation.

cliffs (Aharon et al., 2006). The natural vegetation cover is characterised by dense tropical forest.

Located *ca* 490 km north of the Tropic of Capricorn, Niue has a tropical (Af) climate (Peel et al., 2007), with a mean annual air temperature of 24°C (T_{\min} = 20°C in July, T_{\max} = 29°C in January). Niue receives *ca* 2000 mm of rainfall per year, concentrated between November and April, while the period from May to October is cooler and relatively dry (CSIRO & Australian Bureau of Meteorology, 2011). Rainfall variability is controlled by the seasonal movement of the SPCZ (Figure 1). The southward-positioned SPCZ brings convective rainfall during the warm wet season, while the northward shift of the SPCZ results in cool and drier conditions. Due to its location near the south-western margin of the SPCZ, Niue is sensitive to sea surface temperature and atmospheric circulation changes linked to interannual ENSO dynamics (CSIRO & Australian Bureau of Meteorology, 2011). El Niño events are associated with a north-eastward displacement of the SPCZ, resulting in drier conditions in Niue, particularly during the normally wet austral summer season (Figure 1A). During La Niña events, the SPCZ shifts *ca* 1–3° towards the south-west, leading to increased rainfall in Niue (Figure 1B) (Lorrey et al., 2012; Brown et al., 2020). Between 1969 and 2010, at least one or two tropical cyclones have hit Niue each wet season (CSIRO & Australian Bureau of Meteorology, 2011). During El Niño years, above-average sea surface temperatures in the central and western equatorial Pacific enforce positive cyclonic vorticity (Vincent et al., 2011), resulting in an increase in the frequency of tropical cyclones (CSIRO & Australian Bureau of Meteorology, 2011).

Pioneering work by Aharon et al. (2006) highlighted the potential of speleothems from Niuean caves as palaeoclimate archives. Initial investigations on the controls of dripwater geochemistry suggest meteoric water from the South Pacific is the source of dripwater $\delta^{18}\text{O}$ signatures in Niuean caves (Tremaine et al., 2016), while two main sources of carbon control the $\delta^{13}\text{C}$ in dripwater, including the soil CO_2 and the isotopic signal of the host rock of the carbonate platform (Aharon et al., 2006). Using AMS radiocarbon dating assays and petrographic analyses, Rasbury and Aharon (2006) demonstrated the annual nature of stalagmite laminae, which consist of alternating thick and clear bands growing during the wet season and thin and dark bands that grow during the dry season.

The remote location of Niue Island makes it difficult to collect continuous geochemical data over longer periods; currently, there is little data on rainwater and dripwater stable isotopes available for Niue and neighbouring islands. There is a need for additional data that can help elucidate isotope variability in meteoric waters and support the stalagmite proxy interpretation. This is especially

relevant for storm-derived rainfall, which potentially contributes a significant portion of effective moisture that reaches the caves, thereby leaving a mark in the speleothem oxygen isotope record.

Two palaeoclimate reconstructions have highlighted the sensitivity of Niue Island speleothems as recorders of regional rainfall variability. The first is a record of the SPCZ between 45 ka BP and 25 ka BP (Sinclair et al., 2014), while the second provides an ENSO record over *ca* 200 years from 1750 to 2000 AD (Rasbury & Aharon, 2006). This work builds upon and confirms earlier work and contributes to the knowledge of the tropical Pacific palaeoclimate with a new seasonally resolved record of an unrepresented time period (mid-Holocene).

3 | MATERIALS AND METHODS

3.1 | Stalagmite C132

Stalagmite C132 was collected in the 1970s by Chris Hendy (University of Waikato) from Mataga Cave, between the villages of Tuapa and Hio on the west coast of Niue Island. The stalagmite was found broken in a small grotto at the end of the cave, with the top segment of the stalagmite missing. Due to the collection history of stalagmite C132 and the remote location of Niue Island, it is unlikely that replication material will be found from the same or neighbouring caves covering the same time interval. The collected stalagmite fragment is 43.4 cm long (Figure 2) with visible layers of milky-white pale porous calcite (PPC) and dark dense calcite (DDC). The description of the characteristics of the layers is based on thin section observations and follows the terminology in Hartland et al. (2014).

Stalagmite C132 was sliced vertically using a rock saw at the University of Waikato, resulting in a central slab of *ca* 2 cm thickness and two sides stored as archive halves. The central slab surface closest to the stalagmite growth axis was used for all analyses. Powder samples were obtained for geochemical analyses using a Sherline micro-drill with a 1 mm diameter tungsten-carbide drill and a digital read-out. Eleven powder samples of *ca* 200 mg were collected for U/Th dating. Stable isotope samples were drilled every 3 mm (low resolution, $n=144$) and milled every 50 μm (high resolution, $n=5102$) following the methodology outlined in Baldini et al. (2021). Figure 2 shows the sampling tracks.

3.2 | Image processing

Greyscale values were extracted from high-resolution (2400 dpi) scans of the stalagmite surface along the

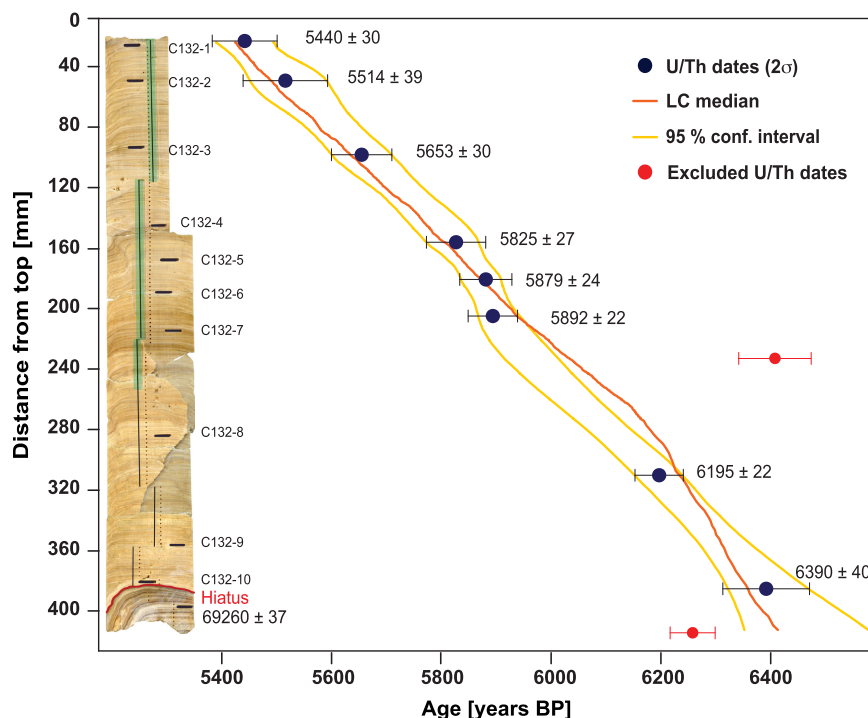


FIGURE 2 Age-depth model of the Holocene section of stalagmite C132. Dark blue circles indicate $^{230}\text{Th}/\text{U}$ -ages with their $\pm 2\sigma$ errors. Red circles indicate excluded $^{230}\text{Th}/\text{U}$ -ages and their $\pm 2\sigma$ errors. The orange line indicates the layer counting median profile, and the yellow lines indicate the 95% confidence intervals. The image of sample C132 shows the U/Th sampling locations (black bars), LA-ICP-MS tracks and greyscale (black lines), the sampling trench for high-resolution stable isotopes (green shading) and low-resolution stable isotope sample locations (dots).

vertical growth axis using the image analysis software ImageJ version 1.51k (<https://imagej.nih.gov/ij/index.html>; Schneider et al., 2012). The scans were taken with HP Scanjet series 2200c flatbed scanner. This analysis provides a record of intensity between zero (black) and 237 (white), with a spatial resolution of $10.6\mu\text{m}$. Assuming the deposition of the PPC and DDC lamina couplets was annual, the greyscale record was used to count the grey value minima corresponding to the DDC laminae, thus constructing a layer counting chronology to constrain the age model and growth rate profile. The annual growth rate was calculated from the difference in distance between a DDC trough (i.e. a minimum value) and the next trough. The layer counting chronology was obtained by both visually counting lamina (using a high-resolution scan) and by counting greyscale peaks extracted from the digital scan. The sensitivity of greyscale values was subsequently tested as an environmental proxy (see section 6.1).

3.3 | U/Th dating and age-depth modelling

The U/Th ages were determined using a Nu Instruments plasma multicollector inductively coupled mass spectrometer (MC-ICP-MS) at the University of Melbourne. Sample powders were dissolved and equilibrated with a $^{229}\text{Th}/^{233}\text{U}$ mixed spike solution before U and Th were separated from the matrix using Eichrom TRU-Spec resin. The purified U/Th fraction was introduced to the MC-ICP-MS via a Cetac Aridus membrane desolvator, giving

total system efficiencies of *ca* 0.3% for both elements. See Hellstrom (2003) for further protocol details.

The age-depth model of stalagmite C132 was initially constrained using eight U/Th ages as inputs in the COPRA age-modelling software (Breitenbach et al., 2012). This U-series-based age-depth model was then further constrained by the layer counting chronology. The series of counted layers versus stalagmite depth was anchored to the depth of the uppermost U/Th date (sample ID C132-1, Table S1). This layer chronology fell within the 2σ uncertainties of the older U/Th dates. This procedure leaves an overall error margin of ± 20 years. The final age model is the median record based on an ensemble of 2000 Monte Carlo age-depth realisations derived from the layer counted profile using the COPRA routine (Breitenbach et al., 2012).

3.4 | Speleothem geochemistry

The resolution of the analysed samples for oxygen and carbon stable isotopes varies from $50\mu\text{m}$ to 3 mm. The first set ($n=607$) of samples covering the depth ranges of 4–16.25 mm and 46.85–92.26 mm was measured at Ruhr University, Bochum. Between $90\mu\text{g}$ and $110\mu\text{g}$ of sample powder was acidified with orthophosphoric acid at 70°C and reacted for 60 min before analysis. The released CO_2 gas was dried and measured in continuous flow mode on a ThermoFisher MAT253 gas source isotope ratio mass spectrometer coupled to a GasBench II (ThermoScientific, Bremen, Germany). Results are

presented in delta notation, with δ -values reported as parts per thousand (‰) relative to the international Vienna PeeDee Belemnite (VPDB) standard. Results are corrected using a two-point calibration using the international standards IAEA-603 and NBS18. The long-term 1σ reproducibility of the internal standard is 0.06‰ for $\delta^{13}\text{C}$ and 0.09‰ for $\delta^{18}\text{O}$.

A second set ($n=740$) of isotope measurements, covering the depth ranges of 92.35–205.26 mm and 16.84–47.16 mm, was performed at ETH Zurich using a ThermoFinnigan Delta V Plus isotope ratio mass spectrometer coupled to a ThermoScientific Gasbench II. Between 90 μg and 140 μg of sample powder were reacted with orthophosphoric acid at 70°C for 60 min. The resulting CO_2 was then sampled and transported in a helium stream to the mass spectrometer. See Breitenbach and Bernasconi (2011) for details on the method. Reference materials include the international standards NBS19 and NBS18. The long-term 1σ reproducibility of the internal standard is 0.05‰ for $\delta^{13}\text{C}$ and 0.08‰ for $\delta^{18}\text{O}$.

The third set ($n=765$) of isotope measurements, from 205.32 to 255.92 mm, was performed at Northumbria University using a ThermoFinnigan Delta V Plus isotope ratio mass spectrometer coupled to a ThermoScientific Gasbench II. In total, 2162 stable isotope samples have been analysed.

Concentrations of 15 elements were measured along the vertical growth axis of stalagmite C132, following the greyscale track. Measurements were performed at the University of Waikato (New Zealand) by laser ablation-inductively coupled mass spectrometry (LA-ICP-MS) using a RESOLUTION SE 193 nm excimer laser ablation system equipped with a Laurin Technic S155 laser ablation cell coupled to an Agilent 8900 QQQ-ICP-MS. Analyses were conducted using a laser repetition rate of 20 Hz with a 60 μm diameter ablation spot and scanning the sample at 29.55 $\mu\text{m}/\text{s}$ with a beam energy density of 5 J/cm², yielding a spatial resolution of 30 μm . Signals for ²³Na, ²⁴Mg, ²⁷Al, ²⁹Si, ³¹P, ³⁴S, ⁴⁴Ca, ⁵⁵Mn, ⁵⁶Fe, ⁶⁰Ni, ⁶³Cu, ⁶⁶Zn, ⁸⁸Sr, ¹³⁷Ba, ²⁰⁸Pb and ²³⁸U were monitored during analysis in a single track. The ICP-MS was optimised daily for maximum sensitivity. The ICP-MS operating settings are: forward power of 1350 W, plasma gas flow rate of 15 L/min (Ar), carrier gas flow of 0.99 mL/min (nebuliser), sampling depth of 4 mm, pulse counting detector and peak hopping sweep mode, 0.01–0.1 s dwell time and one point per peak. Calcium was used as an internal standard, assuming a concentration of 40.04 wt%. Background counts (He gas background, measured with the laser off) were collected for 45 s between samples. The National Institute of Standards and Technology (NIST) glass standards 612 and 610 were analysed after every sample track (*ca* 3 cm

long) to account for any drift. Raw data were processed using Iolite v3.32 (Paton et al., 2011). Background counts were subtracted from the raw data, and all data were standardised to NIST 612, while NIST 610 was utilised as a secondary standard. The GeoReM database (Jochum et al., 2005) was used for NIST glass reference values.

3.5 | Water chemistry

Rainwater and dripwater samples from four Niue caves (Palaha Cave, Anapala Cave, Ulupaka Cave and Avaiki Cave) were collected in a fieldwork campaign in February 2020. The oxygen and hydrogen isotope ($\delta^{18}\text{O}$ and δD) ratios were measured using cavity ring-down spectroscopy (CRDS; Steig et al., 2014) at the Universidad de Almería, Spain. The CRDS device was interfaced with an A0211 high-precision vapouriser. The internal standards were JRW, BOTTY and SPIT. The results were normalised to VSMOW (Vienna Standard Mean Ocean Water). Typical long-term instrumental precisions ($\pm 1\text{SD}$) were $\pm 0.06\text{‰}$ for $\delta^{18}\text{O}$ and $\pm 0.6\text{‰}$ for δD , based on the repeated analysis of an internal standard every six samples.

3.6 | Statistical analyses

3.6.1 | Principal component analyses

Principal component analysis allows the identification of associations of the proxy time series that explain most of the observed variability. Several PCAs were carried out on different groupings of datasets derived from stalagmite C132. The arrangement of the groups is based on the inclusion of different proxy time series, their length and resolution. Principal component analysis-1 includes trace elements, greyscale and growth rate time series; PCA-2 includes trace elements, greyscale, growth rate and stable isotopes time series; and PCA-3 includes trace elements only. All records included in each PCA were standardised to the lowest resolution in the group by averaging the data corresponding to each lowest-resolution time interval to accommodate the differences in temporal resolution. Data preparation prior to PCA analysis included filling in missing values using the iterative PCA algorithm from the missMDA library in the software R and log-transformation to account for non-normality of the data series. The PCAs were performed in the software R using the PCAshiny algorithm from the Factorshiny (v.2.2) package.

The PCA-1 analysis was performed in two separate datasets that correspond to two intervals; this is because the trace element data have a gap at 276.22–281.66 mm (6.219–6.213 ka BP) caused by technical difficulties during

the measurement process. The trace element data above the gap have a substantially higher variance compared to those below the gap. To avoid potential instrumental biasing, the trace element time series was split into two sets and PCAs were performed separately on the upper and lower sections (PCA-1a and PCA-1b). The PCA-2 analysis included the data for the time interval in which $\delta^{18}\text{O}$ and $\delta^{13}\text{C}$ values are available and also included greyscale, trace elements and grow rate. The PCA-3 analysis, including only trace elements, is presented in the Supplement (S2).

3.6.2 | Seasonality determination

The term ‘rainfall seasonality’ is used here to refer only to the difference in the amount of rain between the wet and dry seasons within one annual cycle, as measured by the difference in the greyscale values between a PPC lamina and the adjacent DDC lamina. For the study of mid-Holocene rainfall seasonality, a minor recalibration was performed on the monthly-scale dating of the greyscale record. Based on mean rainfall being higher during the wet season (November–April) compared to the dry season (May–October), the greyscale record was anchored on its time axis such that wet season averages are higher than dry season averages in the maximum possible number of years, yielding a (constant) shift of +5 months. Rainfall seasonality was afterwards calculated for each year as the difference between average greyscale values in the wet and dry seasons.

3.6.3 | Wavelet analysis

To investigate which environmental processes drive the variability recorded in this C132 dataset, the biwavelet package was applied in R to perform wavelet power spectrum analyses using Morlet wavelets (Torrence & Compo, 1998) on the annually resolved greyscale record, the seasonality record and the two first PCs derived from PCA-2. The continuous wavelet analysis of the greyscale record utilised linear interpolation with an annual sampling period. Irregular sampling in the time dimension results in variations in the number of samples per year, biasing estimates of mean season-specific rainfall, a problem that is not resolved by interpolation. Significance testing of wavelet power was thus based on Monte Carlo sampling of AR(1)-realisations computed by the REDFIT algorithm (Schulz & Mudelsee, 2002) to obtain an individual 95% confidence level for each time instance and period. The same procedure was applied to the seasonality time series by transforming each AR(1)-surrogate into a ‘seasonality-surrogate’.

4 | RESULTS

4.1 | Greyscale record

Greyscale intensity varies between 93 and 273 (Figure 3A), with a mean value of 179.4. The PPC laminae have higher values than adjacent DDC laminae. The greyscale record has the highest resolution (10.6 μm) of all C132 proxy records and exhibits variability at seasonal to multi-decadal timescales. The growth rate record reveals a notable change in average growth rate at ca 6.1 ka BP, with faster growth prior to 6.1 ka BP (0.5 ± 0.05 mm/year) and slower growth (0.34 ± 0.01 mm/year) between 6.1 ka BP and 5.4 ka BP (Figure 3F).

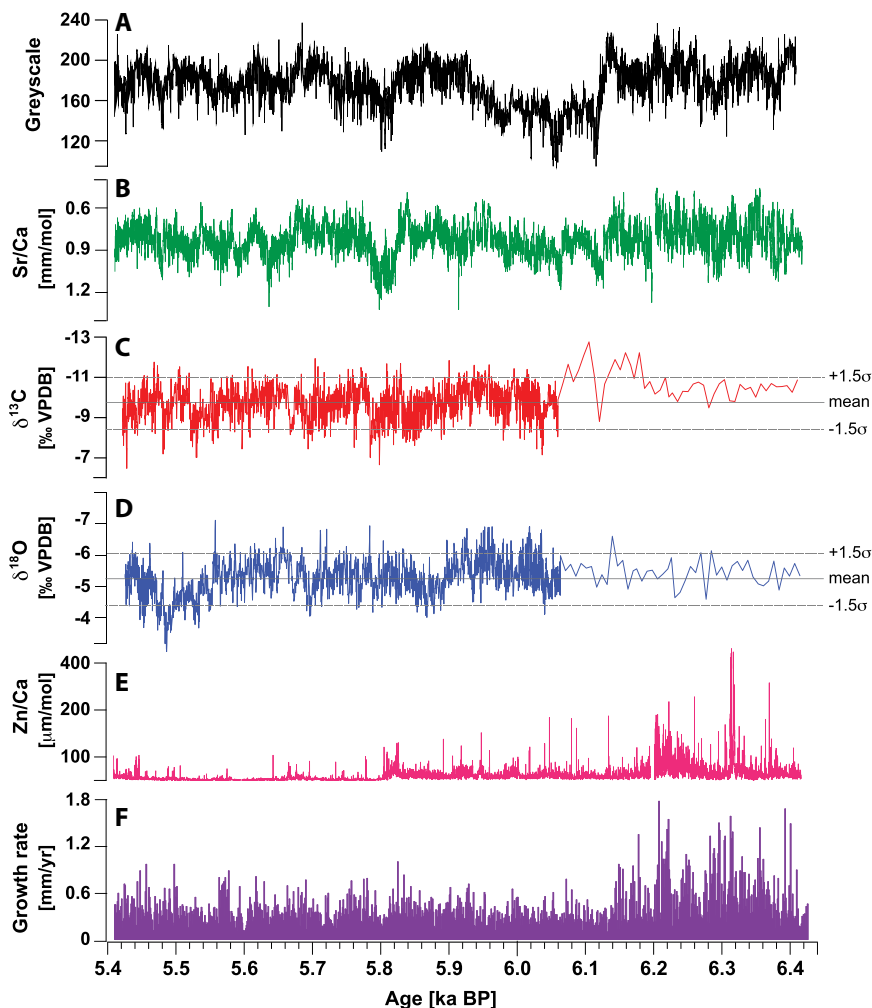
4.2 | U/Th dating and age modelling

Of 11 measured U/Th ages, two were discarded due to large uncertainties, and a third measured sample was not included in this work because it is outside the period of interest in this research (69.3 ka BP); see Table S1. The age model of stalagmite C132 was based on the remaining eight U/Th ages (Figure 2). The final age model is constrained by the youngest radiometric date 5.411 ka BP and the oldest radiometric date 6.428 ka BP (with present referring to 1950 CE), indicating that the stalagmite grew continuously at an average growth rate of 0.39 ± 0.01 mm/year. The Holocene U-series chronology is further refined by layer counting based on the greyscale information. The layer count is within the uncertainties of the U-series dates, suggesting that the layers represent annual banding due to strongly seasonal growth conditions in the cave (Figure 2). Proxy reconstructions are therefore based on the layer counting chronology, anchored to the youngest U/Th date (C132-1). The layer count indicates that the Holocene part of the record spans 1019 years.

4.3 | Speleothem geochemistry

In total, 47 stable isotope samples from the older stalagmite segment (6.411–6.172 ka BP) were measured at low (multi-annual) resolution, and 2279 samples were measured at sub-annual resolution from the younger segment (6.168–5.423 ka BP). Over the analysed interval (6.411–5.423 ka BP), $\delta^{18}\text{O}$ values varied between -7.2‰ and -3.5‰ , with a mean of -5.58‰ (Figure 3D; $n = 2326$). The $\delta^{13}\text{C}$ values ranged from -12.8‰ to -6.5‰ , with a mean of -9.73‰ (Figure 3C; $n = 2326$). The $\delta^{18}\text{O}$ and $\delta^{13}\text{C}$ time series record sub-annual to centennial-scale changes. The $\delta^{18}\text{O}$ and $\delta^{13}\text{C}$ values are positively correlated ($r = 0.58$, $p < 0.001$), with both isotope systems varying synchronously throughout

FIGURE 3 Proxy time series obtained from stalagmite C132. (A) greyscale; (B) Sr/Ca; (C) $\delta^{13}\text{C}$; (D) $\delta^{18}\text{O}$; (E) Zn/Ca; (F) grow rate record. Different temporal resolution has been achieved for $\delta^{13}\text{C}$ and $\delta^{18}\text{O}$ before and after 6.070 ka BP.



the record (Supplement S1). The majority of the stable isotope values fluctuate within $\pm 1.5\sigma$ of the mean. The highest $\delta^{18}\text{O}$ values are found between 5.50 ka BP and 5.46 ka BP, when a decadal-scale positive excursion of *ca* 1.3‰ is recorded. This excursion is followed by a rapid decrease towards the mean (Figure 3D). A similar trend is observed in the $\delta^{13}\text{C}$ record, although in this case the values are much closer to the mean.

High-resolution trace element data allows the detection of sub-annual variability (Figure 4C,E), with values reported as metal/Ca ratios and summarised in Table S2. This section focusses on Sr and Zn variations, which represent contributions from the host rock and the soil, respectively (Figure 3B,E; Aharon et al., 2006; Murgulet, 2010). The host rock elements that reflect PCP are Mg, Sr and Ba because they can substitute for Ca in the carbonate crystal (Fairchild & Treble, 2009). Here, Sr/Ca ratios are used as a proxy for PCP. The Sr/Ca ratios vary between 0.46 mmol/mol and 1.32 mmol/mol, with a mean value of 0.81 mmol/mol (Figure 3B; $n = 14,584$). Since the Mg/Ca ratios (Table S2) are found to be affected by (minor) contributions of dolomite in the host rock, the Mg/Ca ratios were not used as a proxy for PCP. The Zn/Ca ratios range

from 0.1 to 420 $\mu\text{mol/mol}$, with a mean of 17.95 $\mu\text{mol/mol}$ (Figure 3E; $n = 14,567$). Technical difficulties resulted in a small gap in the trace element time series at 276.22–281.66 mm (6.213–6.219 ka BP).

4.4 | Water chemistry

The analysed rainwater shows $\delta^{18}\text{O}$ values that vary between -11.03‰ and -5.49‰ , and δD values ranging from -80.86 and -35.29‰ VSMOW (Figure 5 and Table S3). All rainwater $\delta^{18}\text{O}$ and δD values are near the Global Meteoric Water Line (GMWL, $\delta D = 8 \times \delta^{18}\text{O} + 10$; Craig, 1961) and the South Pacific Meteoric Water Line (SPMWL, $\delta D = 7.7 \times \delta^{18}\text{O} + 9.3$) as determined from rainfall at the Western Samoa and Rarotonga stations (IAEA/WMO, 2001). The rainwater isotopes fit the regression $\delta D = 8.1 \times \delta^{18}\text{O} + 8.6$ and show no secondary evaporation effects. The isotopic composition of the dripwaters collected in the four Niue caves show $\delta^{18}\text{O}$ values from -4.87‰ to -3.97‰ , and δD values between -28.09‰ and -20.34‰ VSMOW. All dripwater $\delta^{18}\text{O}$ and δD values fall on the SPMWL (Figure 5).

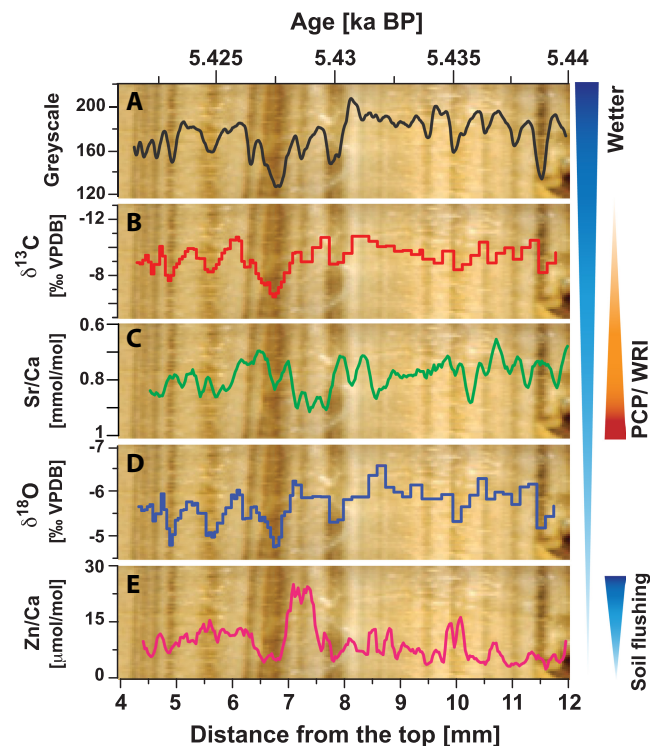


FIGURE 4 Detailed view of an 8 mm section of stalagmite C132 with proxy records superimposed on the stalagmite image, showing the relationship of the proxies with the alternation between pale porous calcite (PPC) and dark dense calcite (DDC) laminae. (A) greyscale, (B) $\delta^{13}\text{C}$, (C) Sr/Ca, (D) $\delta^{18}\text{O}$, (E) Zn/Ca. The $\delta^{13}\text{C}$ and $\delta^{18}\text{O}$ frequently increase in line with lower grey values, while the seasonal-scale dynamics of other proxies are less obvious. For an explanation of the arrows on the right-hand side, see the discussion section.

4.5 | Statistical analyses

Figure 6 displays the PCA results, where each dot signifies the loading of the respective record onto principal components (PCs) 1 and 2. For PCA-1a, the first two PCs explain 56.48% of the variance in the original data (Figure 6A). Zinc, Mn, Fe, Pb, Al, Ni and Cu show a strong positive correlation with PC1 (loadings >0.7) and a moderately positive correlation with PC2 (loadings <0.6). Magnesium, U, Sr and P define a group that is moderately negatively correlated with PC2 (loadings <0.6) and weakly to moderately positively correlated with PC1 (loadings <0.5). The first two components of PCA-1b explain 61.64% of the total variance and show similar associations of elements (with Br added to the second group) and similar correlations to the two PCs as in PCA-1a.

The PCA-2 analysis produces similar groupings to PCAs-1a and -1b but also indicates a third group including Ba, Na and Br (green shading, Figure 6C) and is moderately positively correlated to both PC1 and PC2 (loadings <0.6). The stable isotopes do not contribute to PC1 and

PC2; instead, they present high loadings for PC4. In both PCA-1 and PCA-2, the greyscale record is projected onto the lower left quadrant of the coordinate system spanned by the PCs, indicating an inverse relationship to the group of elements Sr, Mg, U and P. Full-resolution PCAs of trace element data (PCA-3a and b) were also performed with similar results (Supplement S2).

The wavelet spectrum of the greyscale record displays significant power ($>95\%$ confidence level) in the ENSO band (2–8 years), which is mostly continuous throughout the recorded period, with the exception of two brief interruptions at 6.15 and 6.02 ka BP (Figure 7). The wavelet spectra of PC1 and PC2 of PCA-2 show irregular patches of significant periodicities associated with ENSO-band variability at 6000–5950, 5700–5650 and 5500–5400 years BP (Supplement S3).

5 | DISCUSSION

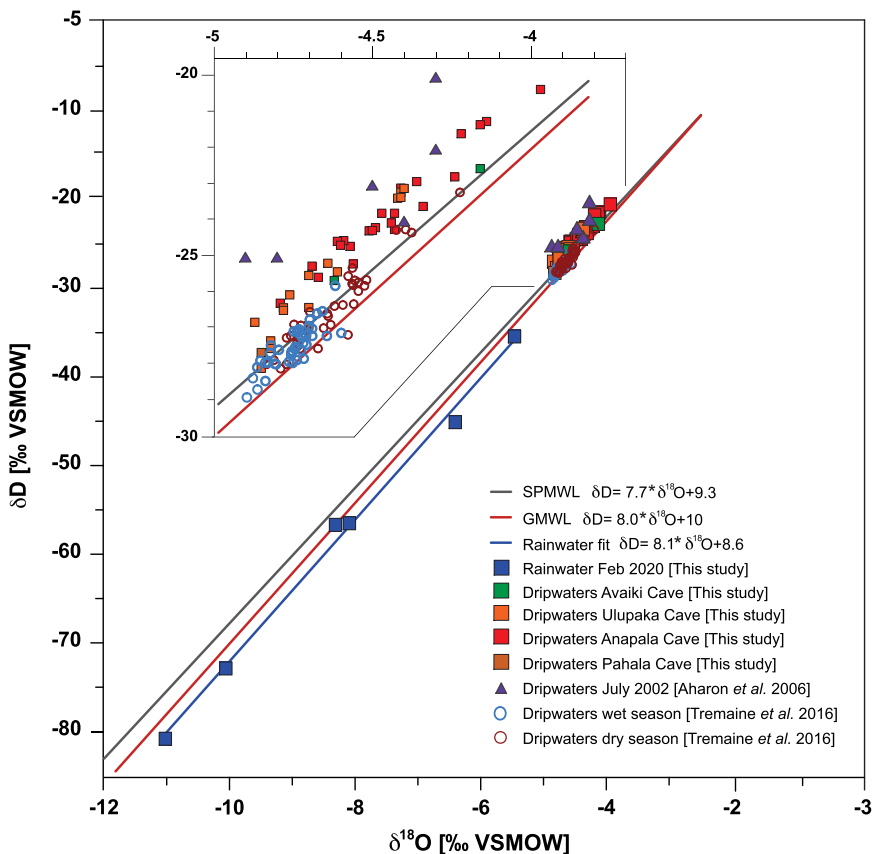
5.1 | Greyscale record as an environmental proxy

The greyscale variability in stalagmite C132 reflects the alternation between PPC and DDC laminae, which is related to crystal growth and matrix-density variation. In the absence of detrital particles (clay, silt or soot) in the speleothem, higher greyscale values represent crystal growth arrangements with more interstitial space and crystal boundaries that reflect light. Lower greyscale values result from denser calcite crystal patterns that reflect less light in reflected light scan images (Figure 4A). Factors such as dripwater saturation, drip rate and CO_2 degassing promoted by cave ventilation govern the formation of distinctive crystal fabrics depending on seasonal environmental conditions (Baker et al., 2008; Frisia, 2015).

Previous work on the petrography of speleothems from Niue has shown laminae composed of columnar calcite crystals parallel to the grow axis. The laminae consist of couplets of alternating thick and clear bands deposited during the wet season and thin and dark bands deposited during the dry season (Aharon et al., 2006). Rasbury and Aharon (2006) used in situ observations, AMS radiocarbon dating and 92 years of monthly rainfall data to verify the annual growth of the band couplets and calculated a growth rate of 0.34 ± 0.04 mm/year. Observations in stalagmite C132 confirm the same laminae growth pattern and similar average growth rate (0.39 ± 0.01 mm/year).

The variations in crystal growth pattern (and thus greyscale values) are interpreted here as primarily a function of the dissolved inorganic carbon (DIC) supply. During the wet season, the supply of dripwater (and with it DIC) is high, allowing for rapid CaCO_3 deposition. In

FIGURE 5 Relationship between $\delta^{18}\text{O}$ and δD of Niue rain and dripwater collected in February 2020. Dripwater samples were collected from Anapala Cave (inland), Palaha Cave (sea cave), Ulupaka Cave (inland) and Avaiki Cave (sea cave). Dripwaters reported in previous studies by Aharon et al. (2006) are shown as triangles and those from Tremaine et al. (2016) as circles (with different colours for wet and dry seasons). The collected samples show no signs of secondary evaporation and plot along the GMWL and SPMWL, which is based on rainfall data of neighbouring Western Samoa and Rarotonga stations (IAEA/WMO, 2001).



the dry season, water supply is more restricted, drip rates are lower and thinner, denser, darker carbonate laminae form. It is suggested here that the mechanism that promotes seasonal signals in the C132 proxy record is the seasonal cycle in dripwater supersaturation, leading to sub-annual changes in stalagmite growth rate. These factors produce seasonal variations in geochemical proxy records in fast-growing speleothems (Hartland et al., 2014; Carlson et al., 2018).

5.2 | Climate interpretation of geochemical proxies

5.2.1 | Stable isotopes as recorders of local environmental conditions

Sub-annual $\delta^{18}\text{O}$ variability observed in stalagmite C132 is attributed to seasonal changes in rainfall and infiltration amount. Due to the small size of Niue Island and its geographical location, the source of the precipitation is entirely oceanic. The summerly southward movement of the SPCZ and tropical cyclones bring strong vertical convective rainfall with a highly negative $\delta^{18}\text{O}$ signature (for example in February 2020, Figure 5).

Presented here are the oxygen and carbon stable isotope values from rainwater and dripwater that were

collected in a single dry season month (February 2020). While this 1-month dataset does not allow to discuss seasonal changes in the isotopic composition of precipitation, it provides valuable information on the isotopic signal of the rainwater transferred to the cave in the island's karst system. The meteoric origin of the dripwaters on Niue Island has been shown in previous studies by Aharon et al. (2006) and Tremaine et al. (2016). Ranging from -4.87‰ to -3.97‰ VSMOW, the dripwater $\delta^{18}\text{O}$ values reported here align well with the previously reported ones by Aharon et al. (2006) and Tremaine et al. (2016), which vary between -4.9‰ and -4.2‰ (Figure 5). The dripwater values of samples collected in this study are close to the South Pacific Meteoric Water Line (SPMWL, $\delta\text{D} = 7.7 \times \delta^{18}\text{O} + 9.3$, $R^2 = 0.96$, IAEA/WMO, 2001), which is based on samples from Samoa and Rarotonga rainfall samples (IAEA/WMO, 2001), as well as on the GMWL (Figure 5). This indicates that secondary evaporation did not affect the dripwater samples. Dripwaters show only a limited range (*ca* 1.1‰ for $\delta^{18}\text{O}$ and *ca* 10‰ for δD ; Figure 5), which suggests a proximal source and that mixing in the epikarst reduced the overall isotope variability.

The rainwater samples collected during tropical storm Vicky in February 2020 (nasa.gov/hurricanes/2020/02/) are characterised by very low and variable $\delta^{18}\text{O}$ (*ca* -11 to -5‰) and δD (*ca* -80 to -35‰) values (Table S3), and

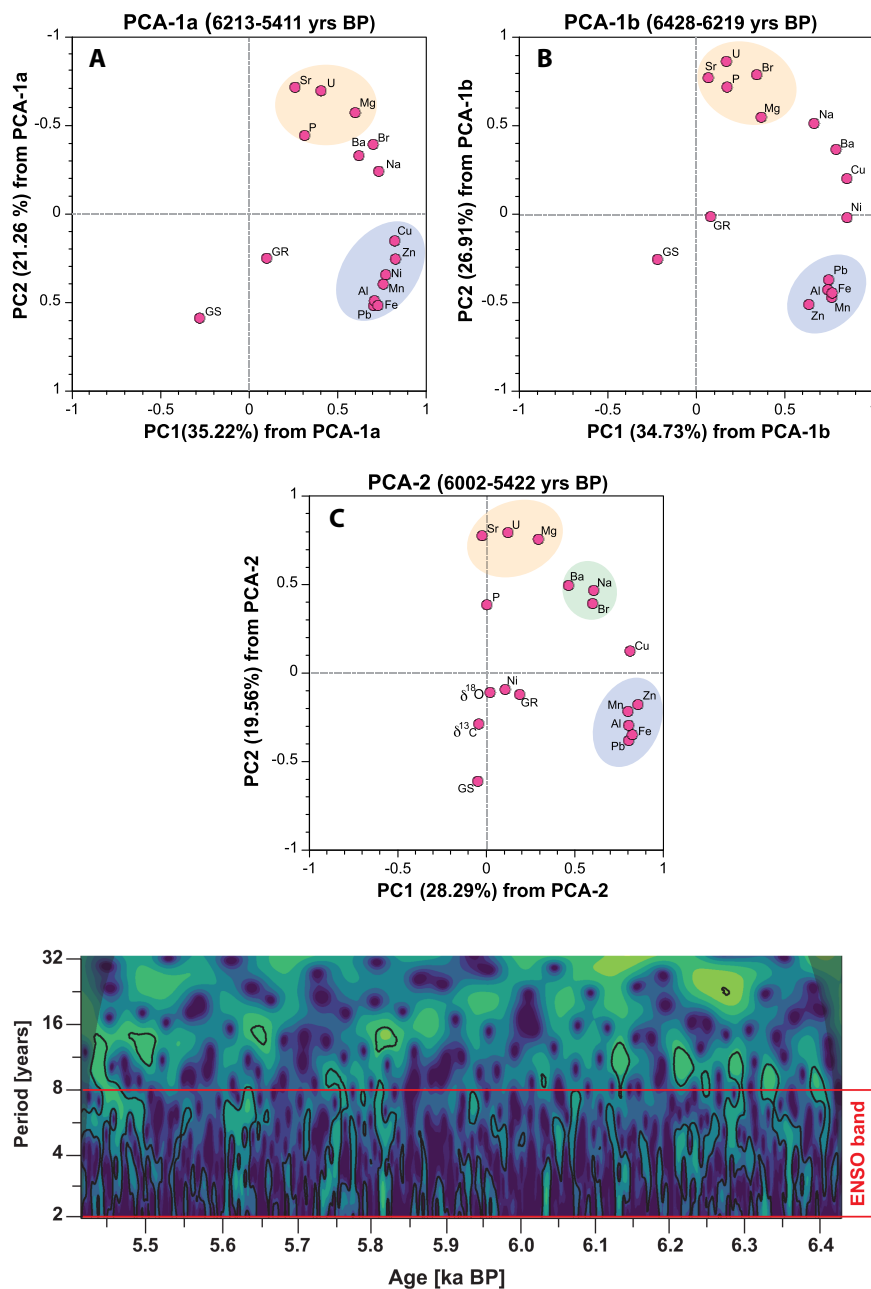


FIGURE 6 Results of the principal component analyses. (A) PCA-1a; (B) PCA-1b; (C) PCA-2. All PCAs reveal two prominent groups: group 1 (blue shaded area) is formed by Zn, Mn, Fe, Pb and Al, and group 2 (orange shaded area) includes Sr, Mg, U and P (except for PCA-2, where P is not included in this group). See Section 5.1 for a time interval explanation. For all PCAs, the data were pre-treated assuming normal distributions after a log-transformation, and all PCAs have annual resolution. Note that in PCA-1a (A), the algorithm assigned the opposite sign to the PC2 axis compared to PCA-1b and PCA-2. This axis is thus reversed for easier comparison.

FIGURE 7 Wavelet spectral analysis of the annually resolved greyscale record from stalagmite C132. Significant (>95%) power is delineated by black contours. The ENSO band (2–8 years) is outlined in red.

are found below the SPMWL and GMWL. These waters form a $\delta^{18}\text{O}$ – δD regression described by the relationship $\delta\text{D} = 8.1 \times \delta^{18}\text{O} + 8.6$ ($R^2 = 0.99$; Figure 5). The similar slope of the collected rainwater samples to that of SPMWL and GMWL indicates condensation under conditions of isotopic equilibrium. The lowest rainwater isotopic values (-72.9 and -80.8‰ for δD , and -10.7 and 11.3‰ for $\delta^{18}\text{O}$) could be explained by the dynamics of tropical storms, whereby convection lifts moist air to greater altitudes where condensation occurs at lower temperature. In addition, the clouds that fed the tropical storm might have experienced enhanced Rayleigh fractionation during more vigorous transport towards the centre of the storm (Sun et al., 2022). Since all dripwater samples are less negative compared to the storm samples, it is suggested here that

the contribution of tropical storm-derived rainwater to the total infiltration is limited. It can be expected, however, that under conditions with increased storm frequency, the dripwater and thus the speleothem $\delta^{18}\text{O}$ signal might respond accordingly.

The dripwater isotope data collected in February 2020 overlap among the four caves (Palaha, Anapala, Ulupaka and Avaiki), suggesting that these samples are representative for the island. The range of observed $\delta^{18}\text{O}$ values is consistent with those reported by Tremaine et al. (2016), who found only a small change of the dripwater $\delta^{18}\text{O}$ signal to lower values in the wet season. Although stalagmite C132 was collected in a different cave, it is suggested that the dripwater isotope values in Mataga Cave are comparable to those reported here and by Tremaine et al. (2016)

due to the spatial proximity of the caves and their shallow depth below ground.

The rainfall isotope signals reflect the seasonal positioning of the SPCZ; during the austral summer season, stronger insolation at the latitude of Niue results in deep and sustained convection and intense rainfall. During the dry season, fewer and weaker low-pressure systems develop. Deep wet season convection also intensifies lateral moisture transport and, thus, Rayleigh fractionation. These processes lead to lower $\delta^{18}\text{O}$ values in wet season rainfall compared to the dry season. The available GNIP data from Rarotonga, collected between May 1979 and November 1991, reveal that wet season (samples from November to April) rainfall $\delta^{18}\text{O}$ averages -5.3‰ , whereas dry season (samples between May and October) rainfall is *ca* 1.4‰ less negative (average $\delta^{18}\text{O} = -3.9\text{‰}$).

Variations in the $\delta^{18}\text{O}$ values of the stalagmite are interpreted here as reflecting seasonal changes in the amount and isotopic composition of the rainfall associated with northern and southern migrations of the SPCZ, and the prevalence of tropical cyclones in the central Pacific. Lower stalagmite $\delta^{18}\text{O}$ values occur in the PPC laminae and reflect the intensity of the wet season, while higher $\delta^{18}\text{O}$ values in the DDC represent the dry season (Figure 4D).

Mechanisms that influence the variability of $\delta^{13}\text{C}$ in speleothems include changes of soil respiration caused by microbial and vegetation activity (Genty et al., 2003; Cruz et al., 2005), the carbon cycle in the ecosystem (Frappier et al., 2002), the changing pH of the infiltrating water leading to intensified water–rock interactions (McDermott, 2004) and PCP (Fohlmeister et al., 2020). In tropical speleothems, the dominant driving force of $\delta^{13}\text{C}$ variations is effective rainfall and drip rate in the cave, as observed in Gupteswar Cave, India or Yok Balum Cave, Belize (Yadava & Ramesh, 2005; Ridley et al., 2015). Stalagmites fed by high drip rates during the wet season present lower $\delta^{13}\text{C}$ values due to the reduced time between drips that limits PCP-related isotope fractionation (Fohlmeister et al., 2020).

The $\delta^{13}\text{C}$ values of stalagmite C132 have a similar range to those of a stalagmite record from nearby Avaiki Cave (Murgulet, 2010). In both records, the $\delta^{13}\text{C}$ values are lower in the wet season (i.e. PPC laminae) and higher in the dry season (DDC laminae; Figure 4B). Aharon et al. (2006) showed that $\delta^{13}\text{C}$ in dripwater in Niue caves represents a mixed signal from both soil CO_2 ($-29.4 \pm 0.09\text{‰}$) and carbonate bedrock ($-0.4 \pm 0.09\text{‰}$). Here, it is inferred that the $\delta^{13}\text{C}$ variations in C132 laminae are caused by changes in the relative proportions of these two carbon sources and, more importantly, by PCP. Lower drip rates during the dry season allow for prolonged CO_2 degassing from the dripwater, enhanced kinetic isotope fractionation and

higher speleothem $\delta^{13}\text{C}$ values in C132 stalagmite. Thus, $\delta^{13}\text{C}$ is interpreted as an indicator of local hydrological conditions within soil and epikarst, with more negative values recorded during wetter periods.

5.2.2 | Elements as tracers of local infiltration dynamics

A series of PCAs were used to investigate the processes controlling trace element variations in stalagmite C132 at annual and sub-annual scales. All PCAs consistently reveal two main groups based on their loadings on PC1 and PC2: Zn, Fe, Cu, Pb, Al and Mn (group 1), and U, Sr, Mg and P (group 2; Figure 6).

Group 1 includes the soil-derived elements that are transported into the epikarst via high-infiltration events (Borsato et al., 2007; Hartland et al., 2012; Oster et al., 2017). Group 2 comprises elements derived from the host rock as well as variable inputs of marine aerosols. This includes Mg and Sr, which are incorporated into the speleothem by water–rock interaction and/or modified by PCP and are often interpreted as proxies for the local hydrology, with higher Mg and Sr concentrations indicating drier conditions (Fairchild & Baker, 2012). Stalagmite C132 Mg/Ca data is not discussed in detail because, although XRD analysis and petrographic observations on thin sections show that the dominant mineral is calcite, trace amounts of dolomite have been identified. This dolomite-related Mg would interfere with the PCP-related signal during calcite precipitation, rendering the measured Mg/Ca values difficult to interpret in terms of infiltration. Instead of Mg/Ca values, the authors believe that the Sr/Ca record better represents the water–rock interactions and PCP processes. This interpretation is corroborated by the similarity of the variability of both greyscale and Sr/Ca ratio records (Figure 3A,B). It is probably that in the epikarst system and stalagmite, the incorporation of U and P into the calcite follows a similar mechanism as observed for Mg that is substitution for CO_3^{2-} in the crystal lattice. Dry periods result in lower host rock dissolution, leading to reduced CO_3^{2-} activity and increased U and P partitioning (Wynn et al., 2018), allowing higher incorporation of U and P in the slower-growing DDC laminae deposited in the dry season. In contrast, higher carbonate supersaturation in the wet season promotes a higher growth rate and increased competition for U and P ions to replace carbonate in the crystal lattice of the PPC laminae (Jamieson et al., 2016).

In all PCAs, Group 2 (host rock-derived) elements show a strongly positive correlation with PC2, which explains between 19.56% and 26.91% of the total variance (Figure 6). Importantly, the greyscale record is moderately

to strongly negatively correlated with PC2, while Group 1 (soil-derived) elements are weakly to moderately negatively correlated with PC2 (Figure 6). Since greyscale values are primarily controlled by dripwater (and thus infiltration) supply, PC2 probably represents the interannual variation between wetter and drier years, with the positive direction indicating drier and the negative direction indicating wetter conditions. Wetter conditions would result in more soil-derived elements being transferred to the cave, leading to the negative correlation with PC2, while host rock-derived elements are concentrated in the calcite during drier conditions due to lower drip rates.

Drier conditions would also concentrate Mg derived from marine aerosols within the epikarst water store, leading to higher Mg/Ca and other element/Ca ratios that are highly concentrated in sea water (e.g. Na, Sr and Ba). It is notable that these elements are separated from the soil-derived elements by PC2 and related to the host rock-derived elements. Thus, while increases in host rock-derived elements (e.g. U, Sr) can be used to identify drier conditions, a similar conclusion would be met if a small contribution of marine aerosol were present. Although this study does not draw on dripwater (chemistry) monitoring, given the marine setting, it is highly probable that marine aerosols also contributed to the elemental composition of C132, similar to earlier findings (Tremaine et al., 2016). This reasoning does not affect the general interpretation of the elemental data.

For all PCA groups, PC1 explains 28–39% of the variance in this dataset. Soil-derived elements of group 1 are strongly positively correlated with this axis, while host rock/marine elements show a weakly positive to no correlation, and greyscale shows a weakly negative to no correlation. Soil-derived elements are transferred to the cave by waterflow through the epikarst. However, overall wet/dry conditions would affect greyscale and host rock-derived elements to a greater and more predictable extent, as discussed above. A key mechanism for the transfer of soil-derived elements is flushing of the epikarst during extreme rainfall events (Hartland et al., 2012), such as tropical cyclones. These events are short-lived and unlikely to have a major effect on the style or rate of (longer-term) calcite crystallisation, thus having a limited effect on greyscale and host rock-derived elements but can import increased soil-derived element loads. PC1 is therefore interpreted as controlled by the prevalence of extreme rainfall events in the tropical Pacific on Niue Island.

With loadings of comparable magnitude on both PC1 and PC2, Na and Br are located between the host rock and soil-derived trace metal groups. As previously noted, Na and Br are concentrated in sea water, and previous studies estimated a sea water contribution of 89% for Na and

Br in the dripwater of Niuean coastal caves (Tremaine et al., 2016). Following this finding, these elements are interpreted as being mostly derived from marine aerosols.

5.3 | Mid-Holocene hydrological variability of Niue Island

5.3.1 | Hydrological patterns on Niue Island

The most prominent driver of seasonal rainfall on Niue Island is the position and strength of the SPCZ. During the austral summer (November–April), the south-westward migration of the SPCZ brings the most rainfall to Niue, while Niue experiences its dry season in the austral winter when the SPCZ migrates north-east. At interannual scale, ENSO dynamics enhance the north/south migrations of the SPCZ and amplify its effect on rainfall amount. During El Niño events, the SPCZ is located further north, thereby making the island drier, and in La Niña events, the SPCZ is located even further south (west), resulting in wetter-than-normal conditions (Figure 1).

An amplified wet season (especially during La Niña events) leads to an increased seasonal contrast in rainfall (i.e. the wet season is wetter-than-normal while the dry season either remains unaltered or is even drier and/or longer) and increased background rainfall. El Niño events, on the other hand, result in a more northerly mean position of the SPCZ and reduced rainfall over Niue Island. Less rainfall during the wet season results in reduced rainfall seasonality as the whole year remains in a dry state (Vincent et al., 2011; Cai et al., 2020; Emile-Geay et al., 2016).

Tropical cyclone activity in the south-western Pacific is also directly linked with ENSO dynamics (Vincent et al., 2011; Cai et al., 2012; Maru et al., 2018). El Niño events are associated with increased tropical cyclone activity (de Scally, 2008). During El Niño years, therefore, Niue Island receives less rainfall overall but more high-infiltration events (CSIRO & Australian Bureau of Meteorology, 2011). This means that rainfall seasonality is less predictable during those years than it is during La Niña events. Therefore, the authors posit three potential hydrological patterns for Niue: El Niño events (low seasonality, low background rainfall, high frequency of high-infiltration events); La Niña events (high seasonality, high background rainfall, relatively lower frequency of high-infiltration events); and ‘normal’ conditions (intermediate seasonality, background rainfall and frequency of high-infiltration events). This mid-Holocene multiproxy record allows detailed insight into these hydrological dynamics at exceptional temporal resolution. In the following, the authors consider longer-timescale patterns

of dominance of one climate state over another. Then evidence for higher-frequency (interannual) variability in ENSO conditions is considered.

5.3.2 | Longer-term (decadal to multicentennial) patterns in climate state

Between 6.4 ka BP and 6.3 ka BP, background rainfall (as reconstructed from PC1; Figure 8A) varies around the average for the record on relatively short (seasonal to decadal) timescales. This period is characterised by high-amplitude variability in high-infiltration events (as reconstructed from PC2; Figure 8B), with some of the highest values in the depositional period. Seasonality in this period is average to low (Figure 8E). These conditions suggest a dominance of normal to El Niño conditions.

From 6.3 to 6.2 ka BP, the record from stalagmite C132 shows high background rainfall (Figure 8A), low frequency of high-infiltration events (Figure 8B) and

high seasonality (Figure 8E). This pattern suggests the dominance of La Niña conditions rather than variability between climate states. This is supported by the relative suppression of significant ENSO-band power in the wavelet spectra of the greyscale and seasonality records (Figure 8F).

From 6.2 to 5.95 ka BP, there is a sustained pattern of lower-than-average background rainfall and a higher-than-average frequency of high-infiltration events (Figure 8A,B). Seasonality is average during the first part of this period and reaches its lowest values during the second part (Figure 8E). Significant power in the ENSO band is seen in the wavelet analysis of the greyscale record but not the seasonality record (Figure 8F). This is interpreted here as a period where ENSO variability was dominated by El Niño to normal conditions.

From 5.95 to 5.75 ka BP, seasonality is relatively high (Figure 8E), background rainfall is high and the frequency of infiltration events is low, suggesting a dominance of La Niña conditions. However, around 5.8 ka BP, although

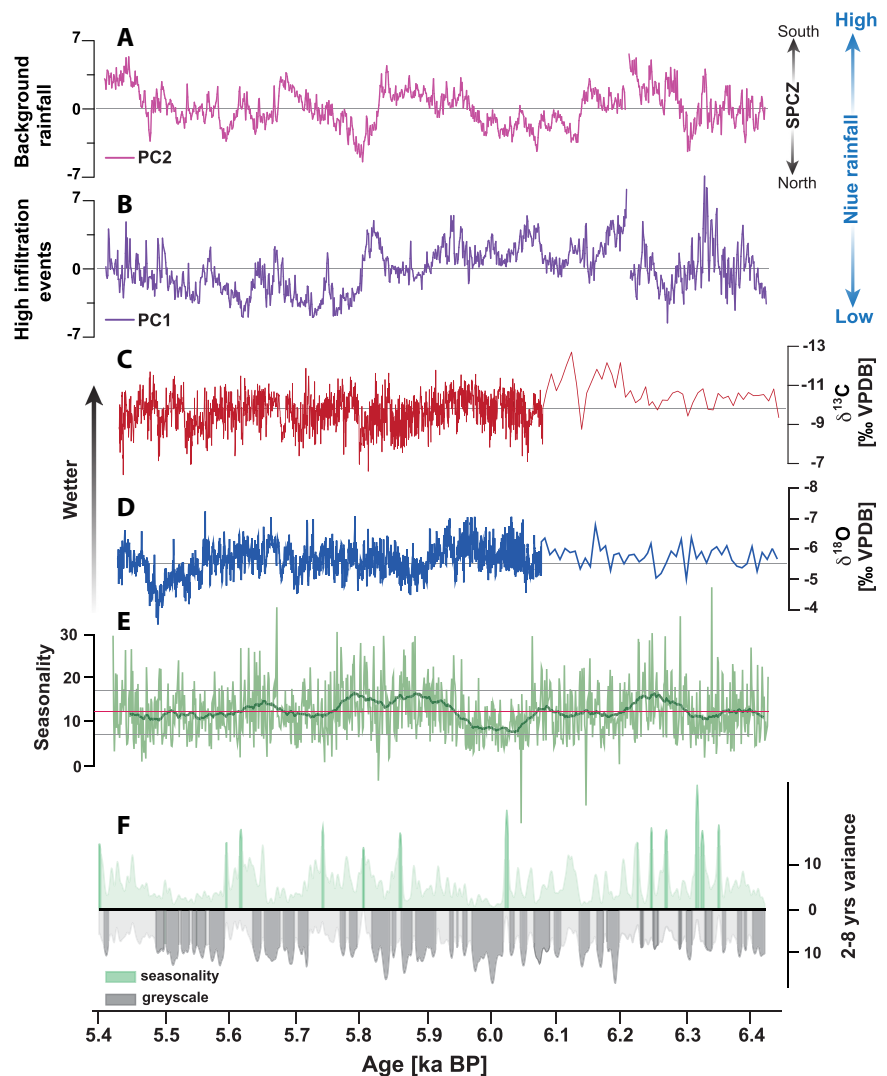


FIGURE 8 (A) Background rainfall (PC2). (B) High-infiltration events (PC1). (C) $\delta^{13}\text{C}$ record. (D) $\delta^{18}\text{O}$ record. (E) Seasonality record extracted from the greyscale record. (F) ENSO-scale variance computed as a 2–8 year wavelet scale average (see Figure 7) from the greyscale record (grey) and seasonality index (green); darker-shaded peaks are above 95% significance.

seasonality remains higher than average, background rainfall drops to some of the lowest values in the record, while the frequency of high-infiltration events rises to some of the highest values in the record. This pattern does not fit with any of the three proposed climate states. Tropical cyclones predominantly occur during the summer (CSIRO & Australian Bureau of Meteorology, 2011); it is therefore hypothesised here that the dominance of El Niño conditions during this period was high enough that tropical cyclone frequency produced a form kind of seasonality signal.

From 5.75 to 5.4 ka BP, the record from stalagmite C132 shows a sustained pattern close-to-average conditions for background rainfall and seasonality, with a low to average frequency of high-infiltration events. This suggests a dominance of the 'normal' climate state. From 5.5 ka BP, background rainfall increases substantially. However, a similar change in the other records is not observed.

5.3.3 | Interannual variability

Figure 8F shows a period when significant power is found in the ENSO band (2–8 years) in wavelet analyses of the seasonality (green) and greyscale (grey) records. This record shows that significant ENSO-band variability occurs across much of the record, indicating that although one of the hydrological patterns, either El Niño or La Niña, may be more dominant on a centennial scale, the interannual variability is still occurring. ENSO-band variability seems to be suppressed in a few periods, most notably around 5.8, 5.75, 5.6 ka BP and from 5.49 to 5.42 ka BP. It is also relatively discontinuous between 6.4 ka BP and 6.2 ka BP. These periods notably coincide with extreme values in background rainfall and/or the frequency of high-infiltration events: 6.4–6.2 ka BP has an elevated frequency of high-infiltration events along with high-amplitude variability; 5.8 ka BP coincides with a peak in high-infiltration events and a trough in background rainfall; 5.75 and 5.6 ka BP both have a low frequency of high-infiltration events, while 5.6 ka BP also has a trough in background rainfall; and the period from 5.49 to 5.42 ka BP has the highest values of background rainfall in the record. This may suggest that during times of unusually high longer-term dominance of either El Niño or La Niña conditions, interannual ENSO variability is suppressed.

Significant ENSO variability in the greyscale record occurs at different periods than in the seasonality record (green and grey peaks in Figure 8F), which suggests different controls. Since the seasonality record reflects wet/dry season contrast, while the greyscale record mostly

reflects the wet season, the authors suggest that the ENSO variability imprint on seasonality is controlled by changes in the amount of rainfall during the dry season, which could either increase or decrease the contrast between seasons. El Niño years are characterised by drier than normal conditions, although tropical cyclones are more frequent (de Scally, 2008). Given that dry season rainfall is generally very low, an overall reduction in dry season rainfall during El Niño years may be counterbalanced by the increased (but erratic) occurrence of tropical cyclones in this season. This would mean that ENSO-scale variability in seasonality might be more probably to occur during periods of dominant El Niño conditions/high frequency of high-infiltration events, as seen in the period 6.4–6.3 ka BP.

These findings suggest that ENSO variability modulates the amplitude of the seasonal rainfall cycle not only at interannual scales but also on multi-decadal and centennial scales. These lower-frequency oscillations could in turn be modulated by (pan-Pacific) long-term stationary states of the mean position of the SPCZ and its spatial configuration, which is controlled by feedbacks of internal mechanisms (Brown et al., 2020).

6 | CONCLUSIONS

The studied stalagmite from Niue Island in the southwestern Pacific offers a seasonally resolved multi-proxy reconstruction of mid-Holocene (6.4–5.4 ka BP) rainfall changes associated with the dynamics of the SPCZ. The combination of U/Th dating and layer counting provides an accurate chronology for the multi-proxy record, while greyscale analysis supports and strengthens the interpretation of the geochemical proxies.

Wet/dry conditions controlled by seasonal shifts of the SPCZ are recorded in the petrography, trace element distribution and isotopic composition ($\delta^{13}\text{C}$ and $\delta^{18}\text{O}$) of the calcite laminae couplets of stalagmite C132. The wet season is reflected in PPC laminae, which are characterised by lower Mg/Ca, Sr/Ca and U/Ca ratios and lower $\delta^{13}\text{C}$ and $\delta^{18}\text{O}$ values. In contrast, the dry season is reflected by DDC laminae with higher Mg/Ca, Sr/Ca and U/Ca ratios and higher $\delta^{13}\text{C}$ and $\delta^{18}\text{O}$ values. The authors suggest that the physicochemical variations in the stalagmite laminae are modulated by kinetic fractionation forced by differences in drip rate and thus stalagmite growth rate between the wet and dry seasons, which in turn depends on the dynamics of the local climate.

Two groups of elements were identified based on the source and mechanism of incorporation into the calcite crystal lattice. Group 1 comprises soil-derived elements (Zn, Mn, Fe, Al and Pb) indicative of high-infiltration

events resulting from extreme but short-lived rainfall events (e.g. from tropical cyclones) that lead to significant soil flushing. The second group includes host rock-derived elements (Mg, Sr, U and P) that are incorporated into the speleothem via water–rock interactions and contributions from marine aerosols. These elements are also sensitive to prior calcite precipitation during periods of reduced infiltration and record hydrological changes at a seasonal scale. This group records lower baseline rainfall during El Niño events and higher baseline rainfall during La Niña events.

Time series and wavelet analyses support the hypothesis of location changes for the SPCZ and provide important insights into ENSO activity during the mid-Holocene. Wavelet analysis suggests that ENSO was continuously active from 6.4 to 5.4ka BP. However, ENSO affects dry-season background rainfall and seasonal rainfall contrast in different ways. It is suggested here that the main effect of this is changes in the overall background rainfall, with La Niña years leading to wetter conditions and El Niño years leading to drier conditions. A secondary effect, related to increased tropical cyclone activity in the dry season during El Niño years, is superimposed on these general dynamics and results in reduced seasonality (wetter dry season and drier wet season).

This interpretation of the climate using proxy records is based on a single stalagmite, and the authors are aware of the challenges that represent the lack of replication and detailed cave monitoring. Nevertheless, this unique seasonally resolved multi-proxy record of tropical Pacific hydrological changes in the mid-Holocene covers an important yet underrepresented time window.

ACKNOWLEDGEMENTS

The authors sincerely thank the Niuean Government and landowners for their generous permission and support of the fieldwork.

FUNDING INFORMATION

This research has been supported by the European Union's Horizon 2020 Research and Innovation programme through a Marie Skłodowska-Curie grant (no. 691037) and aligned funding from Te Apārangi Royal Society of New Zealand (grant no. RIS-UOW1501) and the Rutherford Discovery Fellowship programme (grant no. RDF-UOW1601). Cinthya Nava-Fernandez acknowledges financial support from the German Academic Exchange Service (DAAD). F.G. acknowledges the Ramón y Cajal fellowship, RYC2020-029811-I and the grant PPIT-UAL, Junta de Andalucía-FEDER 2022–2026 (RyC-PPI2021-01).


CONFLICT OF INTEREST STATEMENT

The authors declare that they have no conflict of interest.

DATA AVAILABILITY STATEMENT

All data presented is available at: <https://doi.org/10.5281/zenodo.10146579>.

ORCID

Cinthya Nava-Fernandez  <https://orcid.org/0009-0005-6422-1747>

REFERENCES

- Aharon, P., Rasbury, M. & Murgulet, V. (2006) Caves of Niue Island, South Pacific: speleothems and water geochemistry. In: *Perspectives on Karst geomorphology, hydrology, and geochemistry—a tribute volume to Derek C. Ford and William B. White*, Vol. 404. McLean, Virginia, USA: Geological Society of America, pp. 283–295. [https://doi.org/10.1130/2006.2404\(24\)](https://doi.org/10.1130/2006.2404(24))
- Baker, A., Smith, C.L., Jex, C., Fairchild, I.J., Genty, D. & Fuller, L. (2008) Annually laminated speleothems: a review. *International Journal of Speleology*, 37(3), 193–206. <https://doi.org/10.5038/1827-806x.37.3.4>
- Baldini, J.U.L., Lechleitner, F.A., Breitenbach, S.F.M., Van Hunen, J., Baldini, L.M., Wynn, P.M., Jamieson, R.A., Ridley, H.E., Baker, A.J., Walczak, I.W. & Fohlmeister, J. (2021) Detecting and quantifying palaeoseasonality in stalagmites using geochemical and modelling approaches. *Quaternary Science Reviews*, 254, 106784. <https://doi.org/10.1016/j.quascirev.2020.106784>
- Borsato, A., Frisia, S., Fairchild, I.J., Somogyi, A. & Susini, J. (2007) Trace element distribution in annual stalagmite laminae mapped by micrometer-resolution X-ray fluorescence: implications for incorporation of environmentally significant species. *Geochimica et Cosmochimica Acta*, 71(6), 1494–1512. <https://doi.org/10.1016/j.gca.2006.12.016>
- Braun, T., Breitenbach, S.F.M., Skiba, V., Lechleitner, F.A., Ray, E.E., Baldini, L.M., Polyak, V.J., Baldini, J.U.L., Kennett, D.J., Pruffer, K.M. & Marwan, N. (2023) Decline in seasonal predictability potentially destabilized Classic Maya societies. *Communications Earth & Environment*, 4(82), 1–12. <https://doi.org/10.1038/s43247-023-00717-5>
- Breitenbach, S.F.M., Adkins, J.F., Meyer, H., Marwan, N., Kumar, K.K. & Haug, G.H. (2010) Strong influence of water vapor source dynamics on stable isotopes in precipitation observed in Southern Meghalaya, NE India. *Earth and Planetary Science Letters*, 292(1–2), 212–220. <https://doi.org/10.1016/j.epsl.2010.01.038>
- Breitenbach, S.F.M., Rehfeld, K., Goswami, B., Baldini, J.U.L., Ridley, H.E., Kennett, D.J., Pruffer, K.M., Aquino, V.V., Asmerom, Y., Polyak, V.J., Cheng, H., Kurths, J. & Marwan, N. (2012) COConstructing Proxy Records from Age models (COPRA). *Climate of the Past*, 8(5), 1765–1779. <https://doi.org/10.5194/cp-8-1765-2012>
- Breitenbach, S.F.M. & Bernasconi, S.M. (2011) Carbon and oxygen isotope analysis of small carbonate samples (20 to 100 µg) with a GasBench II preparation device. *Rapid Communications in Mass Spectrometry*, 25(13), 1910–1914. <https://doi.org/10.1002/rcm.5052>
- Brown, J.R., Lengaigne, M., Lintner, B.R., Widlansky, M.J., Van der Wiel, K., Duthiel, C., Linsley, B.K., Matthews, A.J. & Renwick, J. (2020) South Pacific Convergence Zone dynamics, variability

- and impacts in a changing climate. *Nature Reviews Earth and Environment*, 1(10), 530–543. <https://doi.org/10.1038/s43017-020-0078-2>
- Cai, W., Lengaigne, M., Borlace, S., Collins, M., Cowan, T., McPhaden, M.J., Timmermann, A., Power, S., Brown, J., Menkes, C., Ngari, A., Vincent, E.M. & Widlansky, M.J. (2012) More extreme swings of the South Pacific Convergence Zone due to greenhouse warming. *Nature*, 488(7411), 365–369. <https://doi.org/10.1038/nature11358>
- Cai, W., McPhaden, M.J., Grimm, A.M., Rodrigues, R.R., Taschetto, A.S., Garreaud, R.D., Dewitte, B., Poveda, G., Ham, Y., Santoso, A., Ng, B., Anderson, W., Wang, G., Geng, T., Jo, H., Marengo, J.A., Alves, L.M., Osman, M., Li, S., Wu, L., Karamperidou, C., Takahashi, K. & Vera, C. (2020) Climate impacts of the El Niño–Southern Oscillation on South America. *Nature Reviews Earth and Environment*, 1(4), 215–231. <https://doi.org/10.1038/s43017-020-0040-3>
- Cane, M.A. (2005) The evolution of El Niño, past and future. *Earth and Planetary Science Letters*, 230(3–4), 227–240. <https://doi.org/10.1016/j.epsl.2004.12.003>
- Capotondi, A., Wittenberg, A.T., Newman, M., Di Lorenzo, E., Yu, J., Braconnot, P., Cole, J., Dewitte, B., Giese, B., Guilyardi, E., Jin, F., Karaukas, K., Kirtman, K., Lee, T., Schneider, N., Xue, Y. & Yeh, S. (2015) Understanding ENSO diversity. *Bulletin of the American Meteorological Society*, 96(6), 921–938. <https://doi.org/10.1175/BAMS-D-13-00117.1>
- Carlson, P.E., Miller, N.R., Banner, J.L., Breecker, D.O. & Casteel, R.C. (2018) The potential of near-entrance stalagmites as high-resolution terrestrial paleoclimate proxies: application of isotope and trace-element geochemistry to seasonally-resolved chronology. *Geochimica et Cosmochimica Acta*, 235, 55–75. <https://doi.org/10.1016/j.gca.2018.04.036>
- Chen, S., Hoffmann, S.S., Lund, D.C., Cobb, K.M., Emile-Geay, J. & Adkins, J.F. (2016) A high-resolution speleothem record of western equatorial Pacific rainfall: implications for Holocene ENSO evolution. *Earth and Planetary Science Letters*, 442, 61–71. <https://doi.org/10.1016/j.epsl.2016.02.050>
- Cheng, H., Spölt, C., Breitenbach, S.F.M., Sinha, A., Wassenburg, J.A., Jochum, K.P., Scholz, D., Li, X., Yi, L., Peng, Y., Lv, Y., Zhang, P., Votintseva, A., Loginov, V., Ning, Y., Kathayat, G. & Edwards, R.L. (2016) Climate variations of Central Asia on orbital to millennial timescales. *Scientific Reports*, 6(1), 36975. <https://doi.org/10.1038/srep36975>
- Clement, A.C., Seager, R. & Cane, M.A. (2000) Suppression of El Niño during the Mid-Holocene by changes in the Earth's orbit. *Paleoceanography*, 15(6), 731–737. <https://doi.org/10.1029/1999PA000466>
- Cobb, K.M., Westphal, N., Sayani, H.R., Watson, J.T., Di Lorenzo, E., Cheng, H., Edwards, R.L. & Charles, C.D. (2013) Highly variable El Niño–Southern oscillation throughout the Holocene. *Science*, 339(6115), 67–70. <https://doi.org/10.1126/science.1228246>
- Conroy, J.L., Overpeck, J.T., Cole, J.E., Shanahan, T.M. & Steinitz-Kannan, M. (2008) Holocene changes in eastern tropical Pacific climate inferred from a Galápagos lake sediment record. *Quaternary Science Reviews*, 27(11–12), 1166–1180. <https://doi.org/10.1016/j.quascirev.2008.02.015>
- Craig, H. (1961) Isotopic variations in meteoric waters. *Science*, 133(3465), 1702–1703. <https://doi.org/10.1126/science.133.3465.1702>
- Cruz, F.W., Karmann, I., Viana, O., Burns, S.J., Ferrari, J.A., Vuille, M., Sial, A.N. & Moreira, M.Z. (2005) Stable isotope study of cave percolation waters in subtropical Brazil: implications for paleoclimate inferences from speleothems. *Chemical Geology*, 220(3–4), 245–262. <https://doi.org/10.1016/j.chemgeo.2005.04.001>
- CSIRO & Australian Bureau of Meteorology. (2011) Climate change in the Pacific: scientific assessment and new research volume 2: country reports.
- Emile-Geay, J., Cobb, K.M., Carré, M., Breconnot, P., Leloup, J., Zhou, Y., Harrison, S.P., Corrège, T., McGregor, H.V., Collins, M., Driscoll, R., Elliot, M., Schneider, B. & Tudhope, A. (2016) Links between tropical Pacific seasonal, interannual and orbital variability during the Holocene. *Nature Geoscience*, 9(2), 168–173. <https://doi.org/10.1038/ngeo2608>
- Fairchild, I.J., Borsato, A., Tooth, A.F., Frisia, S., Hawkesworth, C.J., Huang, Y., McDermott, F. & Spiro, B. (2000) Controls on trace element (Sr–Mg) compositions of carbonate cave waters: Implications for speleothem climatic records. *Chemical Geology*, 166(3–4), 255–269. [https://doi.org/10.1016/S0009-2541\(99\)00216-8](https://doi.org/10.1016/S0009-2541(99)00216-8)
- Fairchild, I.J. & Baker, A. (2012) *Speleothem Science: from process to past environments*. UK: Wiley-Blackwell. ISBN: 978-1-405-19620-8.
- Fairchild, I.J. & Treble, P.C. (2009) Trace elements in speleothems as recorders of environmental change. *Quaternary Science Reviews*, 28(5), 449–468. <https://doi.org/10.1016/j.quascirev.2008.11.007>
- Faraji, M., Borsato, A., Frisia, S., Hellstrom, J.C., Lorrey, A., Hartland, A., Greig, A. & Matthey, D.P. (2021) Accurate dating of stalagmites from low seasonal contrast tropical Pacific climate using Sr 2D maps, fabrics and annual hydrological cycles. *Scientific Reports*, 11(1), 2178. <https://doi.org/10.1038/s41598-021-81941-x>
- Fohlmeister, J., Voarintsoa, N.R.G., Lechleitner, F.A., Boyd, M., Jacobson, M.J. & Oster, J.L. (2020) Main controls on the stable carbon isotope composition of speleothems. *Geochimica et Cosmochimica Acta*, 279, 67–87. <https://doi.org/10.1016/j.gca.2020.03.042>
- Folland, C.K., Renwick, J.A., Salinger, M.J. & Mullan, A.B. (2002) Relative influences of the Interdecadal Pacific oscillation and ENSO on the South Pacific Convergence Zone. *Geophysical Research Letters*, 29(13), 21–24. <https://doi.org/10.1029/2001gl014201>
- Frappier, A., Sahagian, D., Gonzalez, L.A. & Carpenter S.J. (2002) El Niño events recorded by stalagmite carbon isotopes. *Science*, 298(5593), 565. <https://doi.org/10.1126/science.1076446>
- Frisia, S., Borsato, A., Fairchild, I.J. & McDermott, F. (2000) Calcite fabrics, growth mechanisms, and environments of formation in speleothems from the Italian Alps and Southwestern Ireland. *Journal of Sedimentary Research*, 70(5), 1183–1196. <https://doi.org/10.1306/022900701183>
- Frisia, S. (2015) Microstratigraphic logging of calcite fabrics in speleothems as tool for palaeoclimate studies. *International Journal of Speleology*, 44(1), 1–16. <https://doi.org/10.5038/1827-806X.44.1.1>
- Genty, D., Blamart, D., Ouahdi, R., Gilmour, M., Baker, A., Jouzel, J. & Van-Exter, S. (2003) Precise dating of Dansgaard-Oeschger climate oscillations in western Europe from stalagmite data.

- Nature*, 421(6925), 833–837. <https://doi.org/10.1038/nature01391>
- Hartland, A., Fairchild, I.J., Lead, J.R., Borsato, A., Baker, A., Frisia, S. & Baalousha, M. (2012) From soil to cave: transport of trace metals by natural organic matter in karst dripwaters. *Chemical Geology*, 304–305, 68–82. <https://doi.org/10.1016/j.chemgeo.2012.01.032>
- Hartland, A., Fairchild, I.J., Müller, W. & Dominguez-Villar, D. (2014) Preservation of NOM-metal complexes in a modern hyperalkaline stalagmite: implications for speleothem trace element geochemistry. *Geochimica et Cosmochimica Acta*, 128, 29–43. <https://doi.org/10.1016/j.gca.2013.12.005>
- Hellstrom, J. (2003) Rapid and accurate U/Th dating using parallel ion-counting multi-collector ICP-MS. *Journal of Analytical Atomic Spectrometry*, 18(11), 1346–1351. <https://doi.org/10.1039/b308781f>
- IAEA/WMO. (2001) Global network of isotopes in precipitation. The GNIP database.
- Jamieson, R.A., Baldini, J.U.L., Brett, M.J., Taylor, J., Ridley, H.E., Ottley, C.J., Pruffer, K.M., Wassenburg, J.A., Scholz, D. & Breitenbach, S.F.M. (2016) Intra- and inter-annual uranium concentration variability in a Belizean stalagmite controlled by prior aragonite precipitation: a new tool for reconstructing hydro-climate using aragonitic speleothems. *Geochimica et Cosmochimica Acta*, 190, 332–346. <https://doi.org/10.1016/j.gca.2016.06.037>
- Jochum, K.P., Nohl, U., Herwig, K., Lammel, E., Stoll, B. & Hofmann, A.W. (2005) GeoReM: a new geochemical database for reference materials and isotopic standards. *Geostandards and Geoanalytical Research*, 29(3), 333–338. <https://doi.org/10.1111/j.1751-908x.2005.tb00904.x>
- Kendall, A.C. & Broughton, P.L. (1978) Origin of fabrics in speleothems composed of columnar calcite crystals. *Journal of Sedimentary Research*, 48(2), 519–538. <https://doi.org/10.1306/212F74C3-2B24-11D7-8648000102C1865D>
- Koutavas, A., de Menocal, P.B., Olive, G.C. & Lynch-Stieglitz, J. (2006) Mid-Holocene El Niño–Southern Oscillation (ENSO) attenuation revealed by individual foraminifera in eastern tropical Pacific sediments. *Geology*, 34(12), 993–996. <https://doi.org/10.1130/G22810A.1>
- Koutavas, A. & Joanides, S. (2012) El Niño–Southern Oscillation extrema in the Holocene and last glacial maximum. *Paleoceanography*, 27(4), PA4208. <https://doi.org/10.1029/2012PA002378>
- Lachniet, M.S. (2009) Climatic and environmental controls on speleothem oxygen-isotope values. *Quaternary Science Reviews*, 28(5–6), 412–432. <https://doi.org/10.1016/j.quascirev.2008.10.021>
- Lorrey, A., Dalu, G., Renwick, J., Diamond, H. & Gaetani, M. (2012) Reconstructing the South Pacific Convergence Zone position during the Presatellite Era: a La Niña case study. *Monthly Weather Review*, 140(11), 3653–3668. <https://doi.org/10.1175/MWR-D-11-00228.1>
- Magiera, M., Lechleitner, F.A., Erhardt, A.M., Hartland, A., Kwiciczen, O., Cheng, H., Bradbury, H.J., Turchyn, A.V., Riechelmann, S., Edwards, L. & Breitenbach, S.F.M. (2019) Local and regional Indian summer monsoon precipitation dynamics during termination II and the last interglacial. *Geophysical Research Letters*, 46(21), 12454–12463. <https://doi.org/10.1029/2019GL083721>
- Maru, E., Shibata, T. & Ito, K. (2018) Statistical analysis of tropical cyclones in the Solomon Islands. *Atmosphere*, 9(6), 227. <https://doi.org/10.3390/atmos9060227>
- McDermott, F. (2004) Palaeo-climate reconstruction from stable isotope variations in speleothems: a review. *Quaternary Science Reviews*, 23(7–8), 901–918. <https://doi.org/10.1016/j.quascirev.2003.06.021>
- Moy, C.M., Seltzer, G.O., Rodbell, D.T. & Anderson, D.M. (2002) Variability of El Niño/Southern Oscillation activity at millennial timescales during the Holocene epoch. *Nature*, 420(6912), 162–165. <https://doi.org/10.1038/nature01194>
- Murgulet, V. (2010) *Paleoclimate reconstructions over the last century from a tropical speleothem on Niue Island, South Pacific*. Tuscaloosa, Alabama, USA: The University of Alabama. <https://ir.ua.edu/handle/123456789/868>
- Oster, J.L., Sharp, W.D., Covey, A.K., Gibson, J., Rogers, B. & Hari, M. (2017) Climate response to the 8.2 ka event in coastal California. *Scientific Reports*, 7(1), 1–9. <https://doi.org/10.1038/s41598-017-04215-5>
- Paton, C., Hellstrom, J., Paul, B., Woodhead, J. & Hergt, J. (2011) Iolite: Freeware for the visualisation and processing of mass spectrometric data. *Journal of Analytical Atomic Spectrometry*, 26(12), 2508–2518. <https://doi.org/10.1039/c1ja10172b>
- Peel, M.C., Finlayson, B.L. & McMahon, T.A. (2007) Updated world map of the Köppen-Geiger climate classification. *Hydrology and Earth System Sciences*, 11(5), 1633–1644. <https://doi.org/10.5194/hess-11-1633-2007>
- Rasbury, M. & Aharon, P. (2006) ENSO-controlled rainfall variability records archived in tropical stalagmites from the mid-ocean Island of Niue, South Pacific. *Geochemistry, Geophysics, Geosystems*, 7, Q07010. <https://doi.org/10.1029/2005GC001232>
- Ridley, H.E., Asmerom, Y., Baldini, J.U.L., Breitenbach, S.F.M., Aquino, V.V., Pruffer, K.M., Culleton, B.J., Polyak, V., Lechleitner, F.A., Kennett, D.J., Minghua, Z., Marwan, N., Macpherson, C.G., Baldini, L.M., Xiao, T., Peterkin, J.L., Awe, J. & Haug, G.H. (2015) Aerosol forcing of the position of the intertropical convergence zone since ad 1550. *Nature Geoscience*, 8(3), 195–200. <https://doi.org/10.1038/ngeo2353>
- Rodbell, D.T., Seltzer, G.O., Anderson, D.M., Abbott, M.B., Enfield, D.B. & Newman, J.H. (1999) An ~15,000-year record of El Niño-Driven Alluviation in Southwestern Ecuador. *Science*, 283(5401), 516–520. <https://doi.org/10.1126/science.283.5401.516>
- de Scally, F.A. (2008) Historical Tropical Cyclone Activity and Impacts in The Cook Islands. *Pacific Science*, 62(4), 443–459. [https://doi.org/10.2984/1534-6188\(2008\)62\[443:HTCAA\]2.0.CO;2](https://doi.org/10.2984/1534-6188(2008)62[443:HTCAA]2.0.CO;2)
- Schneider, C.A., Rasband, W.S. & Eliceiri, K.W. (2012) NIH Image to ImageJ: 25 years of image analysis. *Nature Methods*, 9(7), 671–675. <https://doi.org/10.1038/nmeth.2089>
- Schulz, M. & Mudelsee, M. (2002) REDFIT: Estimating red-noise spectra directly from unevenly spaced paleoclimatic time series. *Computers and Geosciences*, 28(3), 421–426. [https://doi.org/10.1016/S0098-3004\(01\)00044-9](https://doi.org/10.1016/S0098-3004(01)00044-9)
- Shulmeister, J. & Lees, B.G. (1995) Pollen evidence from tropical Australia for the onset of an ENSO-dominated climate at c. 4000 BP. *The Holocene*, 5(1), 10–18. <https://doi.org/10.1177/095968369500500102>
- Sinclair, D.J., Sherrell, R.M., Rowe, H.D., Wright, J.D., Mortlock, R.A., Hellstrom, J.C., Cheng, H., Min, A. & Edwards, R.L.

- (2014) A speleothem record of South Pacific Convergence Zone dynamics during MIS 3—evidence for non-stationary coupling between the southern tropical Pacific and Greenland? American Geophysical Union, Fall Meeting 2014, abstract id. PP43A-1441. Bibcode: 2014AGUFMPP43A1441S.
- Steig, E.J., Gkinis, V., Schauer, A.J., Shoenemann, S.W., Samek, K., Hoffnagle, J., Dennis, K.J. & Tan, S.M. (2014) Calibrated high-precision ^{17}O -excess measurements using cavity ring-down spectroscopy with laser-current-tuned cavity resonance. *Atmospheric Measurement Techniques*, 7(8), 2421–2435. <https://doi.org/10.5194/amt-7-2421-2014>
- Sun, C., Tian, L., Shanahan, T.M., Partin, J.W., Gao, Y., Piatrunia, N. & Banner, J. (2022) Isotopic variability in tropical cyclone precipitation is controlled by Rayleigh distillation and cloud microphysics. *Communications Earth & Environment*, 3(50), 1–10. <https://doi.org/10.1038/s43247-022-00381-1>
- Timmermann, A., An, S., Kug, J., Jin, F., Cai, W., Capotondi, A., Cobb, K., Lengaigne, M., McPhaden, M.J., Stuecker, M.F., Stein, K., Wittenberg, A.T., Yun, K., Bayr, T., Chen, H., Chikamoto, Y., Dewitte, B., Dommenges, D., Grothe, P., Guilyardi, E., Ham, Y., Hayashi, M., Ineson, S., Kang, D., Kim, S., Kim, W., Lee, J., Li, T., Luo, J., McGregor, S., Planton, Y., Power, S., Rashid, H., Ren, H., Santoso, A., Takahashi, K., Todd, A., Wang, G., Wang, R., Xie, R., Yang, W., Yeh, S., Yoon, J., Zeller, E. & Zhang, X. (2018) El Niño–Southern Oscillation complexity. *Nature*, 559(7715), 535–545. <https://doi.org/10.1038/s41586-018-0252-6>
- Torrence, C. & Compo, G.P. (1998) A practical guide to wavelet analysis. *Bulletin of the American Meteorological Society*, 79(1), 61–78. [https://doi.org/10.1175/1520-0477\(1998\)079](https://doi.org/10.1175/1520-0477(1998)079)
- Tremaine, D.M., Sinclair, D.J., Stoll, H.M., Lagerström, M., Carvajal, C.P. & Sherrell, R.M. (2016) A two-year automated dripwater chemistry study in a remote cave in the tropical south Pacific: Using [Cl⁻] as a conservative tracer for seasalt contribution of major cations. *Geochimica et Cosmochimica Acta*, 184, 289–310. <https://doi.org/10.1016/j.gca.2016.03.029>
- Tudhope, A.W., Chilcott, C.P., McCulloch, M.T., Cook, E.R., Chappell, J., Ellam, R.M., Lea, D.W., Lough, J.M. & Shimmield, G.B. (2001) Variability in the El Niño–Southern oscillation through a glacial–interglacial cycle. *Science*, 291(5508), 1511–1517. <https://doi.org/10.1126/science.1057969>
- Vincent, E.M., Lengaigne, M., Menkes, C.E., Jourdain, N.C., Marchesiello, P. & Madec, G. (2011) Interannual variability of the South Pacific Convergence Zone and implications for tropical cyclone genesis. *Climate Dynamics*, 36(9–10), 1881–1896. <https://doi.org/10.1007/s00382-009-0716-3>
- Walczak, I.W., Baldini, J.U.L., Baldini, L.M., McDermott, F., Marsden, S., Standish, C.D., Richards, D.A., Andreo, B. & Slater, J. (2015) Reconstructing high-resolution climate using CT scanning of unsectioned stalagmites: a case study identifying the mid-Holocene onset of the Mediterranean climate in southern Iberia. *Quaternary Science Reviews*, 127, 117–128. <https://doi.org/10.1016/j.quascirev.2015.06.013>
- Watanabe, T., Suzuki, A., Minobe, S., Kawashima, T., Kameo, K., Minoshima, K., Aguilar, Y.M., Wani, R., Kawahata, H., Sowa, K., Nagai, T. & Kase, T. (2011) Permanent El Niño during the Pliocene warm period not supported by coral evidence. *Nature*, 471(7337), 209–211. <https://doi.org/10.1038/nature09777>
- White, S.M., Ravelo, A.C. & Polissar, P.J. (2018) Dampened El Niño in the Early and Mid-Holocene due to insolation-forced warming/deepening of the thermocline. *Geophysical Research Letters*, 45(1), 316–326. <https://doi.org/10.1002/2017GL075433>
- Wynn, P.M., Fairchild, I.J., Borsato, A., Spölt, C., Hartland, A., Baker, A., Frisia, S. & Baldini, J.U.L. (2018) Sulphate partitioning into calcite: experimental verification of pH control and application to seasonality in speleothems. *Geochimica et Cosmochimica Acta*, 226, 69–83. <https://doi.org/10.1016/j.gca.2018.01.020>
- Yadava, M.G. & Ramesh, R. (2005) Monsoon reconstruction from radiocarbon dated tropical Indian speleothems. *The Holocene*, 15(1), 48–59. <https://doi.org/10.1191/0959683605h1783rp>

SUPPORTING INFORMATION

Additional supporting information can be found online in the Supporting Information section at the end of this article.

How to cite this article: Nava-Fernandez, C., Braun, T., Pederson, C.L., Fox, B., Hartland, A., Kwiczen, O. et al. (2024) Mid-Holocene rainfall seasonality and ENSO dynamics over the southwestern Pacific. *The Depositional Record*, 10, 176–194. Available from: <https://doi.org/10.1002/dep2.268>